The DOI for this manuscript is doi: 10.1175/JAS-D-16-0312.1

The physics of orographic elevated heating in radiative-convective equilibrium

Shineng Hu

Department of Geology and Geophysics, Yale University, New Haven, Connecticut

William R. Boos

Department of Earth and Planetary Science, University of California, Berkeley, and Climate and Ecosystem Sciences Division, Lawrence Berkeley National Laboratory, Berkeley, California

Corresponding author:

Shineng Hu

210 Whitney Avenue

Kline Geology Laboratory

New Haven, CT 06511

shineng.hu@yale.edu

Tel: 203-909-3201

Abstract

Elevated heating of the atmosphere by large plateaus has been argued to influence regional climate in Asia and other regions, but the mechanisms that cause the troposphere to equilibrate at warmer temperatures over elevated terrain are not well understood. This paper quantitatively describes the physics that controls temperatures over elevated terrain in radiative-convective equilibrium (RCE). First, a cloud system-resolving model (CSRM) is used to simulate RCE states over surfaces with various elevations. Then a theory for the influence of surface elevation on temperatures in RCE is presented. Together with offline radiative transfer calculations, this theory is used to quantitatively attribute the magnitude of the elevated heating effect to top-of-atmosphere radiative flux changes caused by decreases in longwave absorption, shortwave scattering, and the moist lapse rate that occur as surface pressure drops. Sensitivity functions obtained through these offline calculations suggest that elevated heating is weaker in warmer climates, and additional CSRM simulations support this hypothesis. Under certain circumstances, even the sign of the elevated heating effect can change to produce cooler temperatures at a given pressure-level as the surface is lifted in RCE.

1. Introduction

Atmospheric temperature at a given height above sea level is expected to be warmer over an elevated surface than over a non-elevated surface (Molnar and Emanuel 1999, hereafter ME99), a phenomenon sometimes referred to as "elevated heating" (Ye and Wu 1998; Wu and Zhang 1998; Wu et al. 2007). Elevated heating by large plateaus has been argued to drive circulations that influence climate in a broad range of locations. The Bolivian Plateau in South America (Rao and Erdogan 1989), the Colorado Plateau in North America (Tao et al. 1999), the Zagros Plateau in Iran (Zaitchik et al. 2007), and the Tibetan Plateau in Asia (Staff Members of Academia Sinica 1958) have all been claimed to provide thermal forcings for regional monsoons. Even the meridional gradient in surface height on Mars is thought to produce an annual-mean, thermally direct meridional circulation by providing elevated heating (Richardson and Wilson 2002).

Elevated heating has been studied most intensely over the Tibetan Plateau, where the great height and horizontal extent of that surface (4 km and 2.5 million km^2, respectively) were long held to drive the large-scale South Asian summer monsoon (Flohn 1968; Hahn and Manabe 1975; Yanai et al. 1992; Molnar et al. 1993; for a thorough review see Yanai and Wu 2006). The idea that the Tibetan Plateau's elevated heating is strong enough to make it the dominant regional heat source has been recently challenged from both observational and modeling perspectives (Chakraborty et al. 2006; Boos and Kuang 2010; Nie et al. 2010; Ma et al. 2014), but the more fundamental question of what sets the magnitude of the Tibetan Plateau's elevated heating still remains. More generally, how does elevated topography thermally interact with the atmosphere? This question is especially important in the tropics and subtropics, where

topography can set the direction of the incident prevailing wind, and its answer is crucial to understanding the evolution of regional climate on geological time scales.

Answering this question requires a fundamental understanding of the physics of elevated heating by orography, and attaining such an understanding is the central goal of this study. We build on the work of ME99, who showed that temperatures at a given pressure level of the upper troposphere are warmer over elevated surfaces than over non-elevated surfaces in the theoretical state of radiative-convective equilibrium (RCE). In an RCE state, radiative cooling of the atmosphere is balanced by the latent heating of precipitating convection, and there are no temperature or moisture tendencies produced by large-scale flow. Although RCE is never achieved in the real atmosphere, it is nevertheless a conceptually useful state when theoretical and numerical models are employed to understand the radiative and convective physics that influence climate (Emanuel et al. 1994; Held et al. 2007; Romps 2011; Popke et al. 2013; Emanuel et al. 2014; Silvers et al. 2016). Indeed, atmospheric temperatures are sometimes relaxed toward the temperature of the RCE state of a particular column of the atmosphere as a method of forcing idealized simulations of planetary-scale circulations (e.g. Lindzen and Hou 1988; Satoh 1994; Schneider 2006), providing a clean separation between large-scale dynamics and the radiative-convective physics that can be studied in the context of RCE. Here we use the RCE framework to study the mechanism of elevated heating, viewing this as a necessary first step in understanding the complete interaction between radiation, moist convection, and large-scale dynamics over elevated topography.

A variety of mechanisms have been argued to be responsible for the influence of surface elevation on the temperature of the overlying atmosphere, although these have been discussed by only a few authors. Flohn (1953) argued that radiative heating of the surface by solar radiation increases as the surface is lifted because less scattering occurs in a thinner atmosphere, while radiative emission from the surface changes comparatively little. He reasoned that this should produce a warmer atmosphere over mountains than over adjacent non-elevated terrain. ME99 argued that this view is overly simplistic because the rate of atmospheric infrared cooling can change with surface elevation. They also noted that the vertically integrated mass of infrared absorbers might be reduced over an elevated surface, leading to cooling as the local greenhouse effect is reduced. This dependence of the column-integrated mass of infrared absorbers might produce a state-dependence of the elevated heating effect, exemplified by two limiting regimes (ME99): i) the nearly transparent (in the infrared) atmosphere of cold and dry climates would produce only a weak decrease of surface temperature as surface elevation rises, so temperatures at a given pressure-level of the upper troposphere warm strongly as the surface rises; ii) in warm and moist climates with optically thick atmospheres, surface temperatures follow a moist adiabat as the surface is lifted, eliminating nearly all of the elevated heating effect. Although ME99 did find that surface temperature fell as the surface was lifted in their RCE simulations, they did not actually assess the roles played by changes in the vertically integrated mass of infrared absorbers, in clear-sky shortwave scattering (Flohn 1953), or in other processes.

Here we extend the work of ME99 by actually quantifying the influence of various processes on the magnitude of the elevated heating effect. This turns out to be more than a minor incremental effort because we discover that the largest influence on the magnitude of the elevated heating

105 effect is a process not previously discussed: surface temperature drops when the surface is
106 elevated because the moist adiabatic lapse rate decreases as surface elevation rises, leading to
107 stronger longwave cooling of the upper troposphere. This lapse rate effect is similar to the lapse
108 rate feedback discussed in the climate sensitivity literature for greenhouse gas-forced climate
109 change (e.g. Cess 1975; Colman 2003), but is caused by the pressure-dependence of the moist
110 lapse rate rather than by its temperature dependence. We also document the magnitude of several
111 radiative mechanisms by which changes in longwave absorption by greenhouse gases influence
112 the magnitude of elevated heating; these mechanisms have been discussed in the planetary
113 science literature as ways in which the thickness of a planetary atmosphere can affect its
114 equilibrium temperature (e.g. Halevy et al. 2009; Pierrehumbert 2010), but they do not seem to
115 have been discussed in previous studies of elevated heating by orography. Our study also extends
116 the efforts of ME99 in a methodological sense: we simulate RCE states over surfaces of
117 different heights using a cloud system-resolving model (CSRM) in which moist convection is
118 represented explicitly rather than parameterized (ME99 used a single-column model with
119 parameterized convection), and we use offline radiative transfer calculations to better understand
120 the radiative-convective mechanisms that govern the CSRM behavior.
121
122 This paper is organized as follows. The CSRM used in this study and the experimental set-up are
123 described in Section 2. We discuss the elevated heating effect simulated by this model in Section
124 3. We derive an index and present a theory for the elevated heating effect in Section 4. Offline
125 radiative calculations are conducted in Section 5 to quantitatively assess this theory. We further
126 investigate the elevated heating effect across a wide range of climates in Section 6, where we
127 also discuss the possibility that the elevated heating effect can change sign to become elevated

cooling in certain circumstances. We discuss implications and possible directions for future work in Section 7.

2. Numerical model details

We use a CSRM called the System for Atmospheric Modeling (SAM) version 6.3, which solves the anelastic equations of motion with prognostic liquid water moist static energy, total non-precipitating water, and total precipitating water (Khairoutdinov and Randall 2003). We use a horizontal domain size of 96 km × 96 km with 3 km horizontal resolution and 64 vertical levels. This domain has approximately the same size as a single column of a typical global climate model (GCM), so our integrations can be viewed as representative of the state that would be achieved by a single column of a GCM in the absence of any grid-scale horizontal flow between GCM grid cells. Rotation is not included in the equations of motion. Insolation is set to the annual- and diurnal-mean value at 30°N on Earth (~364 W/m^2). We use the radiative transfer scheme from the NCAR Community Climate Model (CCM3; Kiehl et al. 1998). The ozone profile is fixed with respect to the surface, and tropospheric temperatures are relatively insensitive to its changes: for the case with a surface albedo of 0.24 and a surface pressure of 500 hPa, we shifted the ozone profile downward by about 6 km (roughly the height of a 500 hPa surface), and found that equilibrium surface temperature only dropped by half a degree in response.

The lower boundary of the model is an idealized representation of a land surface having a heat capacity equivalent to that of one meter of water. Surface temperature is interactively computed

based on a surface energy balance. Surface fluxes are based on bulk aerodynamic formulae with constant surface exchange coefficients and a constant surface wind speed of 7 m/s. To represent the reduced evaporation that typically occurs over land compared to ocean, we multiply the latent heat flux by a constant fraction $\beta = 0.5$, similar to what was done in ME99. In reality, local feedbacks involving soil moisture and surface relative humidity changes might exist, but are not explicitly considered in our idealized simulations. However, we did test model sensitivity to the surface evaporation fraction: substantial free-tropospheric cooling occurs when β is reduced below 0.25, as expected for a very dry climate, but there is little sensitivity to β for $\beta \geq 0.25$.

In our CSRM simulations, we vary surface pressure, or equivalently surface elevation, at a prescribed surface albedo, and compare the tropospheric temperatures after the system reaches an RCE state. That is, we conduct one simulation for each combination of surface pressure and surface albedo, presenting horizontal and time averages over the last 300 days when the system is in the equilibrium state. We refer to integrations by both surface height and surface pressure, with approximate heights of 0, 1, 2, 3, 4, and 6 km having surface pressures of, respectively, 1008, 890, 790, 710, 600, and 500 hPa. Further description of the experimental set-up is provided in the relevant sections below.

3. Elevated heating in a CSRM

In the first set of experiments, we set surface albedo to 0.24 (near the observed mean for the Tibetan Plateau), and vary surface pressure from 1008 to 500 hPa by roughly 100 hPa increments, as mentioned above. We find that elevated heating, previously found in the RCE

states of a single-column model (ME99), indeed exists in these CSRM simulations that explicitly represent three-dimensional moist convective processes (Fig. 1a). Specifically, surface temperature decreases with surface height, but at a rate of 2.2°C/km that is much slower than typical moist adiabatic lapse rates (6-10°C/km), consistent with the estimate of ME99. As a result, the troposphere is warmer over an elevated surface by as much as 20°C for a 5 km change in surface height, when compared at the same pressure-level.

In a convecting atmosphere, upper-level temperature covaries with subcloud equivalent potential temperature, θ_{eb}, better than it does with surface temperature; this is a central tenet of the theory of convective quasi-equilibrium (CQE; Emanuel et al. 1994). This can be expressed as

$$\delta\theta_{eb} \propto \delta\theta_e^*, \tag{1}$$

where δ represents a variation in time or space, and θ_e^* is the saturation value of the equivalent potential temperature of the convecting layer (θ_e^* depends only on temperature and thus provides an appropriately rescaled measure of temperature; also, for our purposes, equivalent potential temperature could be replaced by moist static energy or moist entropy). When variations in θ_{eb} and θ_e^* are equal rather than simply proportional, the relationship is referred to as strict quasi-equilibrium (SQE). The CQE framework and the SQE assumption have been used extensively in studies of large-scale tropical and monsoon dynamics (Emanuel et al. 1994; Brown and Bretherton 1997; Neelin and Zeng 2000; Nie et al., 2010). Here we find that SQE holds when surface elevation is varied in simulations of RCE. In particular, Fig. 1b shows θ_{eb} plotted against θ_e^* averaged over an upper-tropospheric layer (200-400 hPa), for the same simulations plotted in Fig. 1a and for two additional sets of simulations where surface elevation is fixed at 0 and then at 4 km while surface albedo is varied from 0.22 to 0.40. The points fall very close to the one-to-

197 one line, consistent with the SQE hypothesis. The elevated heating effect can thus be
198 characterized by the effect of surface elevation on θ_{eb} or on upper-tropospheric temperature – the
199 two serve as nearly equivalent metrics. This provides a more convenient and insightful way to
200 use surface air properties to think about the elevated heating effect: one does not need to
201 compare the rate of surface temperature decrease with the moist adiabatic lapse rate, but only
202 assess whether θ_{eb} increases as surface elevation rises. As we discuss in the next section, these
203 two views are equivalent. More generally, one might ask what controls the quantitative
204 sensitivity of θ_{eb} to surface elevation. Is this sensitivity always positive, or might θ_{eb} decrease and
205 the upper-troposphere cool as the surface is lifted?
206
207 **4. Theory**
208
209 **4.1. Derivation of an elevated heating index (EHI)**
210
211 To answer these questions, we first define an elevated heating index (EHI), which is simply the
212 sensitivity of θ_{eb} to surface elevation (z_s),

213 $$EHI \equiv \frac{d\theta_{eb}}{dz_s}. \tag{2}$$

214 In our model and in an atmosphere that can be described by a CQE framework, this index also
215 represents the sensitivity of upper-tropospheric temperature to z_s, as discussed above. Now we
216 express the EHI in terms of other variables by first approximating the subcloud θ_{eb} as the surface
217 air equivalent potential temperature, θ_{es},

218 $$\theta_{eb} \approx \theta_{es} \approx T_s \left(\frac{p_0}{p_s} \right)^{R_d/c_{pd}} \exp\left(\frac{L_v q_s}{c_{pd} T_s} \right). \tag{3}$$

Here q_s is surface air specific humidity, R_d is the gas constant of dry air, c_{pd} is the specific heat at constant pressure of dry air, L_v is the latent heat of evaporation, p_0 is a reference pressure (here taken to be 1000 hPa), and T_s is surface air temperature. Taking the logarithm of each side of Eq. (3) and then differentiating with respect to surface elevation, we obtain

$$\frac{1}{\theta_{eb}}\frac{d\theta_{eb}}{dz_s} \approx \frac{1}{T_s}\frac{dT_s}{dz_s} - \frac{R_d}{c_{pd}p_s}\frac{dp_s}{dz_s} + \left(\frac{L_v}{c_{pd}T_s}\frac{dq_s}{dz_s} - \frac{L_v q_s}{c_{pd}T_s^2}\frac{dT_s}{dz_s}\right). \quad (4)$$

Specific humidity is related to vapor pressure by

$$q_s = \frac{\varepsilon H_s e_s^*}{p_s}, \quad (5)$$

where ε is the ratio of the gas constants for dry air and water vapor, H_s is surface relative humidity (RH), and e^*_s is the saturation vapor pressure of surface air, which depends only on T_s. Assuming that H_s does not change much with surface elevation (Sherwood et al. 2010), which is consistent with our simulations (not shown), changes in specific humidity can thus be due to surface pressure changes or saturation vapor pressure changes. Combining Eqs. (4) and (5), we find

$$\frac{1}{\theta_{eb}}\frac{d\theta_{eb}}{dz_s} \approx \left[1 + \frac{L_v q_s}{c_{pd}}\left(\frac{1}{e_s^*}\frac{de_s^*}{dT_s} - \frac{1}{T_s}\right)\right]\frac{1}{T_s}\frac{dT_s}{dz_s} - \left(1 + \frac{L_v q_s}{R_d T_s}\right)\frac{R_d}{c_{pd}}\frac{1}{p_s}\frac{dp_s}{dz_s}, \quad (6)$$

where part of the last term can be expressed as

$$\frac{1}{p_s}\frac{dp_s}{dz_s} = -\frac{g}{R_d T_s}, \quad (7)$$

using hydrostatic balance and the ideal gas law. Substituting Eq. (7) into Eq. (6), we then find

$$\frac{1}{\theta_{eb}}\frac{d\theta_{eb}}{dz_s} \approx \left(1 + \frac{L_v q_s}{c_{pd}}\frac{1}{e_s^*}\frac{de_s^*}{dT_s}\right)\frac{1}{T_s}\frac{dT_s}{dz_s} + \left(1 + \frac{L_v q_s}{R_d T_s}\right)\frac{g}{c_{pd}T_s}, \quad (8)$$

where we dropped the $1/T_s$ term in square brackets in Eq. (6) because it is more than an order of magnitude smaller than the term involving de^*_s/dT_s. Based on Eq. (8), we obtain the elevated heating index (EHI; defined as $d\theta_{eb}/dz_s$),

$$EHI \approx \frac{\theta_{eb}}{T}\left[\left(1+\frac{L_v q_s}{c_{pd}}\frac{1}{e^*_s}\frac{de^*_s}{dT_s}\right)\frac{dT_s}{dz_s}+\left(1+\frac{L_v q_s}{R_d T_s}\right)\frac{g}{c_{pd}}\right], \tag{9}$$

which can be simplified as

$$EHI \approx A\cdot\left(\frac{dT_s}{dz_s}+\Gamma_{ms}\right), \tag{10}$$

with A a dimensionless number,

$$A=\frac{\theta_{eb}}{T_s}\left(1+\frac{L_v q_s}{c_{pd}}\frac{1}{e^*_s}\frac{de^*_s}{dT_s}\right). \tag{11}$$

The "s" subscript denotes a surface air property, but here and in subsequent offline radiative calculations, we neglect the air-ground temperature difference. The error introduced by this assumption is expected to be small; in our CSRM simulations, the change in air-ground temperature difference produced by surface lifting is about 10% of the change in surface temperature.

The coefficient A is positive definite and state dependent, being larger over high-elevation surfaces (i.e. larger θ_{eb}/T_s) and larger in warmer and moister climates. For example, A equals 2.1 for T_s=15°C and p_s=1000 hPa, and increases to 4.0 either when T_s increases to 32°C or p_s decreases to 500 hPa. The variable Γ_{ms} is

$$\Gamma_{ms}=\left[\left(1+\frac{L_v q_s}{R_d T_s}\right)\Big/\left(1+\frac{L_v q_s}{c_{pd}}\frac{1}{e^*_s}\frac{de^*_s}{dT_s}\right)\right]\frac{g}{c_{pd}}, \tag{12}$$

which has a similar expression to, and here will thus be interpreted as, the moist adiabatic lapse rate evaluated at surface conditions. The only difference with the standard moist lapse rate is the use of specific humidity q_s instead of saturation specific humidity q_s^*, but this has a relatively small effect on Γ_{ms}. More precisely, Γ_{ms} is better interpreted as the moist adiabatic lapse rate at the lifted condensation level (LCL) where the air parcel becomes saturated; in this case the temperature T_s should be replaced with the temperature at the LCL and the EHI represents the sensitivity of θ_e at the LCL to surface elevation.

Eq. (10) is the central result of this subsection, and it intuitively but quantitatively shows the dependence of EHI on the relative magnitudes of the moist adiabatic lapse rate and dT_s/dz_s: upper-tropospheric temperature will be higher over an elevated surface than over a non-elevated surface only if the surface temperature T_s decreases, as z_s rises, more slowly than temperature along a moist adiabat (e.g. Fig. 1a). As is discussed above, the term A in (10) is a proportionality constant that gives the quantitative rate at which θ_{eb} changes with surface height, and it modulates the magnitude of the elevated heating effect simply because here EHI is defined using θ_{eb}; if we instead define EHI using upper tropospheric temperature, the term A will disappear. The terms that control the sign and magnitude of the elevated heating effect are thus the moist adiabatic lapse rate and dT_s/dz_s. The former is easy to estimate given a background climate state, but what controls the sign and magnitude of dT_s/dz_s?

4.2. Two complementary perspectives on elevated heating

When considering how tropospheric temperatures in general respond to surface lifting, one could start by assuming the surface initially either (i) maintains the same temperature it had in the non-elevated case, or (ii) decreases its temperature by following the same pseudoadiabat, with respect to sea level, that existed in the non-elevated case. In either case, surface and tropospheric temperatures will subsequently adjust to a new RCE state, and the details of this adjustment help us understand the mechanisms that set dT_s/dz_s. The two cases correspond to the two extremes depicted in ME99, and will be referred to as the (i) optically thin and (ii) optically thick limits, respectively. In the first limiting scenario, the atmosphere does not interact with radiation, so surface temperature is determined only by insolation, surface albedo, and surface emissivity (i.e. it does not change with surface elevation). In the second case, the atmosphere is optically thick and the RCE moist adiabat remains independent of surface elevation; longwave emission from the lower troposphere does not penetrate to the upper troposphere, so surface lifting has no effect on upper-tropospheric radiative balance. We assume the actual troposphere lies between these limiting cases, so that temperatures will evolve toward a new RCE state after the initial lifting.

If T_s was preserved during lifting [case (i)], the initial state will be too warm compared to the final RCE state, and TOA radiative flux changes produce cooling. As stated in the Introduction, these radiative flux changes might be caused by reductions in the column-integrated mass of infrared absorbers (ME99), but the contribution of this and other changes to the net radiative flux change has not been quantified.

If T_s was decreased during lifting along a pseudoadiabat [case (ii)], the initial state will be too cool and subsequent radiative changes will produce warming. This is because the warm lower

troposphere will have been replaced by a cooler lifted surface, so that if the atmosphere is not strictly in the optically thick limit, OLR will decrease and thus warm the column. This method thus produces "elevated heating" after the initial lifting, providing a useful way of thinking about the phenomenon. However, changes in humidity, the column-integrated mass of dry air, and other atmospheric properties will complicate the response.

As we will show, these two approaches must produce the same final RCE state (assuming multiple equilibria do not exist). We will focus on the first approach (i.e. conducting the initial lifting following the optically thin limit) because it allows us to more easily assess the contributions from different physical mechanisms, including some not discussed by previous studies (Flohn 1953; ME99). However, we will also discuss insights from the second approach (the optically thick limit) below.

4.3. Surface temperature dependence on surface height

We now present a theory for the value of dT_s/dz_s, a quantity sometimes termed the terrestrial lapse rate (Forest et al. 1995; Meyer 2007), and explain how the effect of surface elevation on top-of-atmosphere (TOA) radiative fluxes sets the magnitude, and even the sign, of elevated heating. We use a traditional climate sensitivity framework (Cess et al. 1990; Held and Soden 2000 and references therein),

$$\frac{dT_s}{dz_s} = \left(\frac{\partial R}{\partial z_s} \right)_{T_s} \Big/ \lambda , \tag{13}$$

where R is the net radiative flux at TOA and $\lambda = \left(\partial R/\partial T_s\right)_{z_s}$ is the net climate feedback parameter of the radiative-convective system, representing the sensitivity of TOA radiation to surface temperature changes. In a traditional climate sensitivity calculation (e.g. Cess et al. 1990), such as for a doubling of CO_2, the radiative forcing is imposed and so R can be viewed as the external forcing. Here there is another step in the chain of causation, since R is set by the radiative changes that occur as a consequence of the surface lifting. Although the changes in R and T_s that occur in response to a surface lifting occur simultaneously, we conceptually partition them into two parts: first the surface is lifted without any change in surface temperature and both radiation and moist convection adjust to the new surface elevation, then surface temperature adjusts to the altered net TOA radiation. These two conceptual parts of the response are represented by the numerator and denominator of Eq. (13), respectively, and we now discuss them in sequence.

We decompose the numerator of the right-hand side of Eq. (13) into shortwave and longwave components, and further separate the latter into changes associated with CO_2, H_2O, and lapse-rate effects. We want to emphasize again that surface temperature is fixed as the surface is lifted, but for brevity we drop the subscript T_s on partial derivatives below.

$$\frac{\partial R}{\partial z_s} \equiv \frac{\partial ISR}{\partial z_s} - \frac{\partial OLR}{\partial z_s}$$

$$\approx \frac{\partial ISR}{\partial z_s} - \left(\frac{\partial OLR}{\partial \tau_{CO_2}}\right)_{T,\tau_{H_2O}} \left(\frac{d\tau_{CO_2}}{dz_s}\right) - \left(\frac{\partial OLR}{\partial \tau_{H_2O}}\right)_{T,\tau_{CO_2}} \left(\frac{\partial \tau_{H_2O}}{\partial z_s}\right)_T - \left(\frac{\partial OLR}{\partial T}\right)_{\tau_{CO_2}} \left(\frac{\partial T}{\partial z_s}\right) \quad (14)$$

$$= \mathrm{SW} - \mathrm{LW_{CO2}} - \mathrm{LW_{H2O}} - \mathrm{LW_{LAPSE+H2O}}.$$

In the second line of Eq. (14), τ represents the optical depth of a given constituent, and T represents tropospheric temperature that is controlled by the moist adiabatic lapse rate given a fixed surface temperature. The four terms on the right-hand side of Eq. (14) represent the effect of surface elevation on, respectively, (i) incoming shortwave radiation (ISR) due to changes in clear-sky scattering and absorption by air (labeled in the third line above as SW), (ii) outgoing longwave radiation (OLR) due to changes in the optical depth of carbon dioxide (LW_{CO2}), (iii) OLR due to changes in the amount of longwave absorption by a given mass of water, e.g. the pressure broadening of water vapor's absorption lines (LW_{H2O}), and (iv) OLR due to changes in both the atmospheric lapse rate and the associated vapor pressure needed to keep a fixed RH profile ($LW_{LAPSE+H2O}$).

The first two terms are relatively straightforward to understand. The third water vapor term might seem counterintuitive because it assumes a fixed mass of total precipitable water due to use of the same profiles of T(z), RH(z), and thus $e_s(z)$; it represents changes in absorption due only to pressure effects. The last (fourth) term includes the effects of changes in tropospheric temperature as well as the changes in water vapor that accompany the lapse rate changes, assuming fixed relative humidity. Cloud radiative effects are highly uncertain and not included in Eq. (14), but will be discussed later. To be clear, these four terms represent the effect of changes in surface height on TOA radiation at fixed surface temperature; the resulting change in surface temperature is then found using Eq. (13) as in a traditional climate sensitivity calculation.

The denominator of Eq. (13) can be determined in multiple ways. First, we double CO_2 concentrations in one of our CSRM simulations that has a surface albedo of 0.24 and a surface

366 pressure of 500 hPa, and estimate the climate feedback λ from the CO_2 doubling-induced abrupt
367 changes in TOA radiative fluxes and the equilibrium surface temperature changes. Although the
368 value of λ might be expected to depend on the details of how *R* is perturbed, we find good
369 quantitative agreement between values of λ obtained through different radiative forcings. In the
370 next section we present an alternate estimate of λ calculated for a change in the TOA shortwave
371 induced by varying surface albedo; this turns out to be nearly identical to that produced by CO_2
372 doubling. We emphasize that here λ is an equilibrium climate feedback parameter; the global
373 mean transient climate sensitivity has been shown to vary in time as regions with different
374 surface heat capacities warm at different rates, but even that complication can be explained by
375 assuming climate feedbacks that are linear and constant in time for a particular region (Armour
376 et al. 2013). The value of λ for our simple RCE system additionally seems to have little
377 sensitivity to the nature of *R*, although we have not sampled very dry states or a large range of
378 basic state temperatures.
379
380 **5. Mechanistic attribution with offline radiative calculations**
381
382 Now we use offline radiative calculations to estimate each term in Eq. (14), thereby
383 understanding what sets the magnitude of the elevated heating effect. We use a single-column
384 radiative-convective toolkit called CliMT (Climate Modeling and diagnostics Toolkit; Caballero
385 2012) to quantitatively attribute the net TOA radiative flux change to the processes represented
386 by each term. Like other single-column models, CliMT has no horizontal degrees of freedom; it
387 is vertically discretized into 26 equispaced pressure levels. We take the approach of imposing
388 vertical profiles of temperature, humidity, and CO_2 in the model, then using CliMT to conduct

offline radiative transfer calculations to obtain TOA radiative fluxes. To ease comparison with our CSRM results, we chose the same NCAR CCM3 radiative scheme for CliMT as used in our CSRM (although some details of that scheme's implementation may differ).

We estimate the various partial derivatives in Eq. (14) based on TOA radiative fluxes from a large ensemble of CliMT simulations with different surface temperatures and surface elevations. We start with a set of simulations having non-elevated surfaces (i.e. surface pressure = p_{ref} = 1000 hPa) and vertical temperature profiles that are moist pseudoadiabatic from the specified surface temperature up to the tropopause, defined as the level at which the pseudoadiabat reaches -100°C, with a constant stratospheric temperature of -100°C prescribed above. We used a moist pseudoadiabat starting from the surface instead of from the LCL for the sake of simplicity and consistency with our derivation of the EHI, but expect similar results if a dry adiabat was used below the LCL, as long as the LCL is not very high. The relative humidity profile mimics that in the CSRM simulations and is fixed for all climate sensitivity calculations here: it has a surface value of 69%, local maxima of 87% and 90% at altitudes of 1 km and 15 km above the surface, respectively, a local minimum of 60% at 8 km, is zero above 21 km, and is piecewise linear in between. There are no cloud-radiative interactions. Surface albedo is tuned for each surface temperature to obtain an RCE state (i.e. one in which the net TOA radiative flux is zero). We refer to this as the reference state, with one reference state existing for each value of surface temperature examined. We then lift the surface until its pressure drops to p_{target}, then calculate how the TOA radiative flux, R, changes as a result of that lifting while T_s is held constant (this gives $\left[\partial R/\partial z_s\right]_{T_s}$ in Eq. [13], and it is the climate feedback parameter λ that determines how T_s responds to this change in R after equilibration). This is done for many combinations of T_s and

412 p_{target} (listed in Section 6); for each combination we perform several versions of this calculation
413 to find the various total and partial derivatives in Eq. (14):
414
415 (i) Estimating the first term in Eq. (14), $\partial ISR/\partial z_s$, is straightforward: it is simply the net ISR
416 change at TOA, relative to the reference state, when the surface is elevated while T_s and the CO_2
417 mixing ratio are fixed but other quantities are allowed to change. In particular, the lapse rate is
418 allowed to change (Fig. 2a shows the pressure-dependence of the moist lapse rate) and vapor
419 pressure is modified to maintain fixed *RH(z)*. Changes in clear-sky shortwave absorption by
420 water vapor are included in this estimate but are typically about a factor of 4 smaller than the
421 changes due to scattering by dry air.
422
423 (ii) The second term, which represents the influence of changes in CO_2 optical depth on OLR, is
424 estimated by comparing OLR in two configurations that differ only in their CO_2 concentrations.
425 Each has the same T_s and *T(z)* [with z indicating the height above each surface] as the reference
426 state and uses a lifted surface (with surface pressure p_{target}). One of these configurations uses the
427 same CO_2 mixing ratio as the reference state, while the mixing ratio in the other is increased by a
428 factor of $(p_{ref}/p_{target})^2$ to obtain the same CO_2 optical path as the reference state. Note that the
429 column-integrated mass of CO_2 changes by p_{ref}/p_{target}, but the optical path of CO_2 changes
430 quadratically because of the pressure-broadening of absorption lines (Pierrehumbert 2010). Since
431 water vapor absorption features are also broadened by pressure, we multiplied the vapor pressure
432 in both configurations by a scale factor in order to hold the water vapor optical path constant. We
433 determined this scale factor by varying it iteratively until the OLR difference with the reference
434 state was less than 0.001 W/m2; the factor turns out to be slightly greater than unity.

435

436 (iii) The third term represents the influence of modified water vapor absorption while CO_2
437 optical path, T_s, $T(z)$, and $RH(z)$ are all held constant. This is estimated by comparing OLR for
438 two cases, each with lifted surfaces and with the CO_2 scaled by $(p_{ref}/p_{target})^2$ to obtain the same
439 CO_2 optical path as the reference state. In one case the vapor pressure is set to be the same as in
440 the reference case, while in the other it is scaled by the same factor described in (ii) above to
441 compensate for changes in pressure-broadening. Alternatively, the third term can also be
442 estimated by comparing two cases with different surface pressures but with the same profiles of
443 T_s, $T(z)$, $RH(z)$, and CO_2 optical depth [i.e. scaled by $(p_{ref}/p_{target})^2$]. These two approaches are
444 equivalent and are simply different representations of the derivatives in the third term.
445

446 (iv) The fourth term, which represents the effect of changes in lapse rate and accompanying
447 changes in vapor pressure, is estimated by comparing OLR in two cases, each with lifted
448 surfaces with the same T_s and with CO_2 scaled by $(p_{ref}/p_{target})^2$ to obtain the same CO2 optical
449 path as the reference state. One case uses the same $T(z)$ and vapor pressure as the reference state,
450 while in the other $T(z)$ is modified so that lapse rates are moist adiabatic at the modified surface
451 pressure; vapor pressure is also changed to maintain constant $RH(z)$.
452

453 To directly compare with the conditions used in our main set of CSRM experiments, we now
454 show in Fig. 3 our offline estimates of each term in Eq. (14) for a change in p_s from 1000 hPa to
455 500 hPa and a surface albedo of 0.24, which has a corresponding RCE surface temperature of
456 about 28°C for the non-elevated surface. Using the offline calculations described in items (i) and
457 (ii) above, we find that the increase in absorbed shortwave radiation due to reduced clear-sky

458 scattering is nearly equal to the increase in outgoing longwave radiation due to the reduction in
459 CO_2 optical path (i.e. $SW \approx LW_{CO2}$ in Eq. [14]; note that CO_2 optical depth increases
460 quadratically with p_s, rather than linearly, because of pressure-broadening of its absorption lines).
461 The water vapor line breadth term (LW_{H2O}, the calculation of which is described in item [iii]
462 above) has a cooling effect of similar magnitude to each of the previous two terms, and arises
463 from the fact that a given vertical profile of water vapor pressure has a smaller optical depth
464 when surface pressure is reduced. The largest term $LW_{LAPSE+H2O}$, as far as we know, has not
465 been considered by previous studies of elevated heating and so will now be discussed in detail.
466
467 The $LW_{LAPSE+H2O}$ term in Eq. (14) represents enhanced longwave cooling that results from the
468 reduction in moist adiabatic lapse rate that occurs as p_s drops. It can be understood by
469 considering what happens to R as the surface is elevated with surface temperature and relative
470 humidity fixed. Since vapor pressure depends only on temperature and since p_s decreases, the
471 water vapor mixing ratio increases and thus the moist adiabatic lapse rate is reduced (Fig. 2a).
472 That is, as p_s decreases there is less dry air to be heated by condensation of a given mass of
473 water. As a result, air temperature above the elevated surface will be warmer than air
474 temperature the same distance above the non-elevated surface (e.g. Fig. 2b, where height is
475 referenced in km relative to each surface). The vertically integrated effect of this dependence of
476 the moist adiabatic lapse rate on surface pressure produces a much warmer troposphere above the
477 elevated surface (again, at a given altitude relative to each surface). For surface temperatures of
478 5-15°C, a reduction of surface pressure from 1000 to 500 hPa produces a temperature contrast as
479 large as 10-30°C at altitudes of 10-15 km (Fig. 2c).
480

481 This increase of air temperature at a given altitude above the surface increases OLR, cooling the
482 column. Some of this cooling is offset by the reduction in OLR that occurs as water vapor
483 pressure increases in the warmer upper troposphere, where relative humidity has been argued to
484 stay roughly constant as the lapse rate changes (Sherwood et al. 2010). This lapse rate effect,
485 including the associated water vapor changes, is analogous to that which occurs as CO_2 is
486 increased over a non-elevated surface (Soden and Held 2006). As in that well-known scenario,
487 our calculations show that the net effect of the change in lapse rate is an increase in OLR with
488 surface elevation (i.e. the temperature effect dominates). For the particular case of lifting the
489 surface from 1000 to 500 hPa, the temperature part of the lapse rate effect accounts for -48.1
490 W/m^2 while the associated water vapor effect is +36.7 W/m^2, yielding a total lapse rate effect
491 of -11.4 W/m^2. This net lapse rate effect is larger than any of the other terms discussed above or
492 mentioned in ME99 and, unlike the other terms, it involves both moist convective and radiative
493 processes rather than radiation alone. One could categorize the terms in Eq. (14) differently and
494 add together all the contributions from greenhouse gas changes (LW_{CO2}, LW_{H2O}, and the water
495 vapor component of $LW_{LAPSE+H2O}$), yielding a positive value that would cancel much but not all
496 of the temperature component of $LW_{LAPSE+H2O}$. Note that, as the atmospheric column cools in
497 response to the TOA radiative changes, its pseudoadiabatic lapse rate will adjust accordingly; our
498 framework does not impose an artificially low lapse rate over elevated surfaces.
499
500 For this particular case of lifting the surface from 1000 to 500 hPa with a surface temperature of
501 28°C, we further investigate which levels the lapse rate effect comes from using offline radiative
502 calculations (yellow lines in Fig. 4). Due to the lapse rate change, the whole troposphere is much
503 warmer, and this temperature difference extends to the lower stratosphere. Note that the upper

level warming is realized by a lifted "tropopause" in offline radiative calculations, mimicking the fact that, in the CSRM simulations, the warming always extends to the lower stratosphere before it gradually vanishes with height in the presence of the basic state ozone heating (not shown). Next we eliminate the temperature difference above a certain level in our offline calculation, and study its effect on $LW_{LAPSE+H2O}$ (Fig. 4b). We find that about 60% of the lapse rate effect comes from the lower stratosphere/upper troposphere (e.g. above 100 hPa). However, the contribution from the lower stratosphere/upper troposphere shrinks in colder and drier climates. For example, when for a surface temperature of 20°C, the elimination of air temperature changes above 150 hPa has little effect on the magnitude of $LW_{LAPSE+H2O}$, and the contribution from the mid and lower troposphere dominates (Fig. 4b). Note that the non-monotonic changes with height in Fig. 4b occur because of nonlinear radiative interactions among different vertical levels.

The sum of all four of these individual effects (i through iv above) is -20.9 W/m^2 for our surface lifting from 1000 to 500 hPa. Nonlinearities are slight: simulation in CliMT of the net change in R produced by the same surface lifting while T_s is fixed has a magnitude that is only about 1 W/m^2 smaller (compare black and gray bars in Fig. 3).

To predict the change in surface temperature caused by the surface lifting, we combine this net change in R with the climate feedback parameter λ. As mentioned in the previous section, a doubled-CO_2 CSRM simulation yielded an estimate of λ = 2.5 W/(m^2·K). Although one might think that the climate feedback on a CO_2 doubling could differ substantially from the feedback on a surface lifting, it is important to remember that a change in surface elevation alters surface temperature partly through a change in CO_2 optical depth. To test if the climate feedback

parameter is sensitive to the details of how the TOA radiative fluxes are perturbed, we separately estimated λ in CliMT using two different approaches with the same background state as in the CSRM (surface albedo = 0.24, surface pressure = 500 hPa). In the first approach we doubled CO_2 concentrations just like we did in the CSRM, while in the second approach we examined the surface temperature change caused by a change in surface albedo. The latter provides an estimate of λ based on a shortwave rather than a longwave forcing. We obtained a nearly identical value of λ for these two independent approaches using CliMT: 2.0 W/m^2. The modest differences in λ obtained from the CSRM and from CliMT are expected, given their totally different treatments of convection and the suppressed cloud-radiation interaction in CliMT.

Given this value of λ (i.e. 2.5 W/[m^2·K]), the net change in R of -20.9 W/m^2 in response to a surface lifting from 1000 to 500 hPa is expected to cool the surface by about 8.4 K. This explains about 65% of the 13 K surface temperature drop found in our CSRM (Fig. 1a, where the black dashed line represents our linearized estimate). The remaining one-third of the temperature drop simulated in the CSRM might come from the full complexity of those simulations, e.g. cloud radiative effects, relative humidity changes, deviation of temperatures from moist adiabatic, air-ground temperature difference changes, and radiative transfer details that differ from those of our offline calculations. Note that if we use the CliMT estimate of λ, this climate sensitivity framework can precisely predict the surface temperature dependence on surface elevation in the idealized offline calculations with CliMT (i.e. no cloud radiative effect, fixed relative humidity profile, temperatures following moist adiabats, and no air-ground temperature difference).

549 We now use offline radiative calculations to illustrate the equivalence of the two approaches
550 described in Section 4.2. We again choose a non-elevated surface with albedo of 0.24 and
551 temperature of 28°C, then elevate this surface to 500 hPa. In one case, we fix surface
552 temperature during lifting ($T_{s,ref}$ = 28°C), and in the other, we set the temperature of the elevated
553 surface to the air temperature that existed at 500 hPa in the non-elevated case ($T_{s,ref}$ = 5°C). In
554 both cases, a moist pseudoadiabat (with a minimum of -100°C) and a fixed relative humidity
555 profile are assumed. We then calculate the TOA radiative flux change, ΔR_{TOA}, and estimate the
556 subsequent surface temperature change, $\Delta T_{s,est}=\Delta R_{TOA}/\lambda$, using the climate feedback parameter λ
557 (~2.0 W/[m^2·K]). In both cases, the estimated equilibrium surface temperature $T_{s,est}$ agrees well
558 with the final equilibirium surface temperature $T_{s,eq}$ simulated by the full single-column model
559 (Table 1). A single equilibrium solution is found for $T_{s,eq}$ with no evidence for multiple equilibria.
560 The small discrepancy between the estimated and final equilibrium surface temperature mainly
561 results from the varying climate feedback parameter in different climate states.
562
563 **6. Elevated heating across a wide range of climates**
564
565 We now use our offline radiative-convective calculations together with additional CSRM
566 simulations to characterize the elevated heating effect over a broad range of surface temperatures
567 and surface elevation changes. We begin by repeating the complete set of offline radiative-
568 convective calculations described in the previous section for every T_s between 0 and 40°C, with
569 an interval of 1°C, and for every target surface pressure between 500 and 990 hPa, with an
570 interval of 10 hPa. This allows the magnitude of each term in Eq. (14) to be plotted as a function
571 of T_s and target surface pressure (Fig. 5a-d). For every T_s and p_{target} combination, we also

calculate the net change in R that includes all effects and their interactions (i.e. the surface is lifted and the lapse rate is allowed to change while T_s, CO_2 mixing ratio, and $RH(z)$ are fixed). The sum of all individual terms (i – iv above) is very nearly equal to this net change in R (compare panels e and f of Fig. 5; also see Fig. 3), which shows that the various effects are additive with small nonlinearities; this also lends confidence to our methodology.

The results show that the net change in shortwave has an opposite sign but similar magnitude to the change in OLR that is caused by the modified CO_2 optical path. The shortwave term increases with surface temperature because of the larger ISR associated with the smaller surface albedo required to achieve a warmer RCE reference state (Fig. 5a). It is thus important to remember that the surface temperature dependence of each term shown in Fig. 5 may differ if surface temperature is altered by a forcing other than surface albedo; e.g. the shortwave term may not increase in magnitude if the climate state is warmed by an increase in greenhouse gas concentrations.

The change in OLR due only to pressure-induced changes in water vapor absorption has the same sign and roughly the same magnitude as the CO_2-driven OLR changes. These two terms have little sensitivity to T_s and scale near-linearly with the change in surface pressure (Fig. 5b,c).

The fourth term, which includes all effects of changes in lapse rate, is relatively weak in cold climates but is much stronger than any of the other terms for large changes in surface pressures in warm climates (Fig. 5d). Its sensitivity to T_s is much larger than, and of opposite sign to, that of the shortwave change (Fig. 5a,d). We emphasize again that the lapse rate term includes the

595 direct effect of temperature (e.g. OLR increases as the surface is lifted because the upper-
596 troposphere warms as the moist lapse rate decreases) as well as the compensating effect of
597 moisture (e.g. a reduced lapse rate and fixed RH require an increase in upper-tropospheric vapor
598 pressure and thus a reduction in OLR). Unlike the shortwave term, the temperature-dependence
599 of the lapse rate term is expected to hold regardless of what causes the change in climate state, as
600 long as the vertical temperature profile is strongly constrained by moist convection.
601
602 The combined effects of these four terms, $\left(\partial R/\partial z_s\right)_{T_s}$, is negative and increases in magnitude as
603 the climate warms (Fig. 5e,f), causing an increase in the magnitude of dT_s/dz_s given a constant
604 climate feedback λ. However, the actual dT_s/dz_s change will be affected by the state dependence
605 of λ (e.g. dependence on background temperature or surface elevation), the value of which
606 involves large uncertainty due to cloud-radiative feedbacks and which might furthermore be
607 model dependent. This is an important topic in and of itself, but we leave it for future
608 investigation. At the same time, the moist lapse rate is smaller in warmer climates (Fig. 2a),
609 which directly controls the last term on the right-hand side of Eq. (10). Both factors (i.e. a more
610 negative dT_s/dz_s and a less positive Γ_{ms}) work together to decrease the EHI. The exact value of
611 EHI in our definition is also dependent on the coefficient A in Eq. (11), but as we will show later,
612 the state-dependence of the EHI is dominated by changes in $\left(\partial R/\partial z_s\right)_{T_s}$.
613
614 Since it is clear that $\left(\partial R/\partial z_s\right)_{T_s}$ is dominated by the lapse rate term in the warmest climates (Fig.
615 5d), we now discuss the physics and implications of this effect in greater detail. The OLR change
616 can be linearized as $4\,\sigma T^3 \Delta T$, with σ the Stefan-Boltzmann constant, T the effective emission

temperature, and ΔT the change in temperature at the emission level due to the lapse rate change. As climate warms, the lapse rate change (ΔT) that occurs as the surface is lifted becomes larger in the upper troposphere/lower stratosphere (e.g. Fig. 4a). This increases the OLR change, making dT_s/dz_s more negative in warmer climates and reducing the magnitude of elevated heating (Figs. 4b; 5d).

To confirm the hypothesis that elevated heating weakens in warmer climates, we conduct additional tests using the cloud-system resolving model. Due to computational resource limits, we are not able to explore the wide range of surface temperatures and elevations examined in the offline radiative calculations. Instead, we prescribe surface albedos that range from 0.22 to 0.40 to control the background climate state, and we elevate the surface from 0 km (i.e. 1000 hPa surface pressure) to 4 km (600 hPa surface pressure). We find that the decrease in T_s that occurs as the surface is lifted is larger at lower albedos (Fig. 6a). Also, we find that a given surface lifting produces a smaller increase in θ_{eb} in warmer climates, which confirms that elevated heating is indeed reduced in warmer climates in our CSRM (Fig. 6b). As for the first set of simulations described in Section 3, SQE holds for these simulations and thus θ_{eb} is a good indicator of upper tropospheric temperature (Fig. 1b). These additional CSRM simulations thus confirm our hypothesis, motivated by our theory and offline calculations, that elevated heating is weaker in warmer climates.

Can the elevated heating effect approach zero or even change sign to become elevated cooling? As shown by Eq. (10), the sign of the EHI is determined by the relative magnitudes of the decrease in surface temperature, dT_s/dz_s, and the moist adiabatic lapse rate Γ_{ms}. As illustrated in

Fig. 6a, the former term increases in magnitude and the latter term decreases in warmer climates. Therefore, if the magnitude of dT_s/dz_s exceeds that of Γ_{ms}, elevated cooling will occur.

To achieve a warmer climate state, we set the surface albedo to 0.2 in the CSRM, which is lower than any of the values shown in Fig. 6. At this surface albedo, the system with a non-elevated surface reaches a runaway greenhouse regime because the net downward solar radiation exceeds the upper limit of OLR the system can emit (Ingersol 1969). A runaway greenhouse state is also achieved for surface elevations of 1 km (i.e. 890 hPa surface pressure) at this albedo. However, when we elevate the surface to 1.5 km (i.e. 850 hPa surface pressure), the system achieves an RCE state. Further increasing the surface elevation to 2 km (i.e. 790 hPa surface pressure) produces an RCE state with a cooler troposphere than that in the case with surface elevation of 1.5 km (Fig. 7a,b). Although the temperature at a given pressure level drops by less than 1 K when we lift the surface from 1.5 to 2 km, this clearly shows that one cannot universally expect tropospheric warming as surface elevation increases. In very warm and moist climates, the lapse rate effect in Eq. (14) dominates to produce elevated cooling. This elevated cooling effect (i.e. negative EHI) persists when the CSRM simulations are repeated without radiatively active clouds, showing that it is not dependent on uncertain cloud-radiative effects (Fig. 7c,d).

A possible explanation for this elevated cooling can be found in the perspective of the optically thick limit. In our CSRM simulations, ground temperature is higher than that of the immediately overlying air (i.e. a ground temperature discontinuity exists). In hot, moist climates, OLR might increase in response to surface lifting as radiation from the higher surface penetrates the overlying atmosphere, thus cooling the column.

7. Discussion

Elevated heating produced by the rise of orography has been widely invoked as a forcing for thermally direct circulations that influence regional climate in Earth's tropics and subtropics (e.g. Staff Members of Academia Sinica 1958; Wu et al. 2007). It has also been argued to set some characteristics of the general circulation of the Martian atmosphere (Richardson and Wilson 2002). Yet despite its importance, the physics of elevated heating has not been well understood. For example, no theory existed for the quantitative sensitivities of surface temperature and upper-tropospheric temperature to surface elevation, even in the idealized state of radiative-convective equilibrium.

Here we built on the work of ME99, who used parameterized convection to simulate radiative-convective equilibrium states over surfaces of different elevations. It is intuitive that elevated heating will occur if surface temperature decreases with surface elevation more slowly than the lapse rate of the non-elevated case (barring large compensating changes in air-ground temperature difference); we used a formalization of this idea together with a climate sensitivity framework to understand the radiative-convective processes that set the magnitude and sign of the elevated heating effect. In particular, we showed that the magnitude and sign of the elevated heating effect are set by top-of-atmosphere radiative changes dominated by the sensitivity of the moist adiabatic lapse rate to surface height. Based on the quantitative characteristics of this lapse rate feedback, we hypothesized that surface temperature should decrease more rapidly with surface elevation in warmer climates, and thus elevated heating should be weaker in warmer

686 climates. This hypothesis is supported by offline radiative calculations and is further confirmed
687 by cloud-system resolving simulations. In a sufficiently warm climate, elevated heating can even
688 change sign to become elevated cooling.
689
690 Much work remains to be done to connect our results with real climate states where large-scale
691 dynamics interact with radiative-convective processes, and where surface albedo and soil
692 moisture may be influenced by surface elevation. For instance, observations show a faster
693 warming trend during the last 50 years over the Tibetan Plateau compared with its lower-
694 elevation surroundings (e.g. Mountain Research Initiative EDW Working Group 2015). This
695 observed trend might be taken to suggest that elevated heating increases in magnitude in warmer
696 climates, which would contradict our RCE findings. However, the enhanced warming trend at
697 high elevations might be caused primarily by changes in the large-scale circulation, land surface
698 drying, surface albedo reductions due to the melting of snow and ice cover, aerosol changes, and
699 more. We will quantitatively explore in separate work how changes in surface albedo can
700 potentially compensate for the elevated heating effect (Hu and Boos 2017), and hope that other
701 idealized modeling and observational analyses will help in understanding the more general
702 interactions between large-scale dynamics, land surface hydrology, and the radiative-convective
703 physics of elevated heating.
704
705
706 **Acknowledgements**
707

We acknowledge support from National Science Foundation grants AGS-1253222 and AGS-1515960, Office of Naval Research grant N00014-15-1-2531, and the Yale University Faculty of Arts and Sciences High Performance Computing facility. We thank Peter Molnar, Mark Brandon, and Yiqi Zheng for helpful discussions.

712 **References**

713

714 Armour, K. C., C. M. Bitz, and G. H. Roe, 2013: Time-Varying Climate Sensitivity from
715 Regional Feedbacks. *J. Climate*, **26**, 4518–4534, doi: 10.1175/JCLI-D-12-00544.1.
716 Boos, W. R., and Z. M. Kuang, 2010: Dominant control of the South Asian monsoon by
717 orographic insulation versus plateau heating. *Nature*, **463,** 218-222,
718 doi:10.1038/nature08707.
719 Brown, R. G., and C. S. Bretherton, 1997: A test of the strict quasi-equilibrium theory on long
720 time and space scales. *J. Atmos. Sci.*, **54,** 624-638, doi:10.1175/1520-
721 0469(1997)054<0624:ATOTSQ>2.0.CO;2
722 Caballero, R., 2012: CliMT: Climate Modeling and Diagnostics Toolkit. [Available online at
723 https://github.com/rodrigo-caballero/CliMT.]
724 Chakraborty, A., R. S. Nanjundiah, and J. Srinivasan, 2006: Theoretical aspects of the onset of
725 Indian summer monsoon from perturbed orography simulations in a GCM. *Ann.*
726 *Geophys.*, **24**, 2075-2089, doi:10.5194/angeo-24-2075-2006.
727 Cess, R. D., 1975: Global climate change: an investigation of atmospheric feedback mechanisms.
728 Tellus, **27**, 193–198, doi:10.1111/j.2153-3490.1975.tb01672.x.
729 Cess, R. D., et al., 1990: Intercomparison and interpretation of climate feedback processes in 19
730 atmospheric general circulation models, *J. Geophys. Res.-Atmos.*, **95**, 16601–16615,
731 doi:10.1029/JD095iD10p16601.
732 Colman, R., 2003: A comparison of climate feedbacks in general circulation models. *Climate*
733 *Dyn.*, **20**, 865-873, doi:10.1007/s00382-003-0310-z.

734 Emanuel, K., A. A. Wing, and E. M. Vincent, 2014: Radiative-convective instability. *J. Adv.*
735 *Model Earth Sy.*, **6,** 75-90, doi:10.1002/2013MS000270.
736 Emanuel, K. A., J. D. Neelin, and C. S. Bretherton, 1994: On Large-Scale Circulations in
737 Convecting Atmospheres. *Q. J. Roy. Meteor. Soc.*, **120,** 1111-1143,
738 doi:10.1002/qj.49712051902.
739 Flohn, H., 1953: Hochgebirge und allgemeine Zirkulation. II. Die Gebirge als Wa¨rmequellen.
740 *Arch. Meteorol. Geophys. Bioklimatol.*, **A 5**, 265–279.
741 Flohn, H., 1968: *Contributions to a meteorology of the Tibetan Highlands.* Department of
742 Atmospheric Science, Colorado State University.
743 Forest, C. E., Molnar, P., and Emanuel, K. A., 1995: Palaeoaltimetry from energy conservation
744 principles. *Nature*, **374**, 347-350.
745 Hahn, D. G., and S. Manabe, 1975: Role of Mountains in South Asian Monsoon Circulation. *J.*
746 *Atmos. Sci.*, **32,** 1515-1541, doi:10.1175/1520-
747 0469(1975)032<1515:TROMIT>2.0.CO;2.
748 Halevy, I., R. T. Pierrehumbert, and D. P. Schrag, 2009: Radiative transfer in CO2-rich
749 paleoatmospheres, *J. Geophys. Res.-Atmos.*, **114**, D18112, doi:10.1029/2009JD011915.
750 Held, I. M., and B. J. Soden, 2000: Water vapor feedback and global warming. *Annu. Rev.*
751 *Energy Environ.*, **25**, 441–475, doi:10.1146/annurev.energy.25.1.441.
752 Held, I. M., M. Zhao, and B. Wyman, 2007: Dynamic radiative-convective equilibria using
753 GCM column physics. *J. Atmos. Sci.*, **64,** 228-238, doi:10.1175/JAS3825.11.
754 Hu, S., and W. R. Boos, 2017: Competing effects of surface albedo and orographic elevated
755 heating on regional climate, *Geophys. Res. Lett.*, in press, doi:10.1002/2016GL072441.

Ingersol, A. P., 1969: Runaway Greenhouse - a History of Water on Venus. *J. Atmos. Sci.*, **26,** 1191-1198, doi:10.1175/1520-0469(1969)026<1191:TRGAHO>2.0.CO;2.

Khairoutdinov, M. F., and D. A. Randall, 2003: Cloud resolving modeling of the ARM summer 1997 IOP: Model formulation, results, uncertainties, and sensitivities. *J. Atmos. Sci.*, **60,** 607-625, doi:10.1175/1520-0469(2003)060<0607:CRMOTA>2.0.CO;2.

Kiehl, J. T., J. J. Hack, G. B. Bonan, B. A. Boville, D. L. Williamson, and P. J. Rasch, 1998: The National Center for Atmospheric Research Community Climate Model: CCM3. *J. Climate*, **11,** 1131-1149, doi:10.1175/1520-0442(1998)011<1131:TNCFAR>2.0.CO;2.

Lindzen, R. S., and A. Y. Hou, 1988: Hadley Circulations for Zonally Averaged Heating Centered Off the Equator. *J. Atmos. Sci.*, **45,** 2416-2427, doi:10.1175/1520-0469(1988)045<2416:HCFZAH>2.0.CO;2.

Ma, D., W. Boos, and Z. Kuang, 2014: Effects of Orography and Surface Heat Fluxes on the South Asian Summer Monsoon. *J. Climate*, **27**, 6647-6659, doi:10.1175/JCLI-D-14-00138.1.

Meyer, H. W., 2007: A review of paleotemperature–lapse rate methods for estimating paleoelevation from fossil floras. *Reviews in Mineralogy and Geochemistry*, **66**, 155-171.

Molnar, P., and K. A. Emanuel, 1999: Temperature profiles in radiative-convective equilibrium above surfaces at different heights. *J. Geophys. Res.-Atmos.*, **104,** 24265-24271, doi:10.1029/1999JD900485.

Molnar, P., P. England, and J. Martinod, 1993: Mantle Dynamics, Uplift of the Tibetan Plateau, and the Indian Monsoon. *Rev. Geophys.*, **31,** 357-396, doi:10.1029/93RG02030.

Mountain Research Initiative EDW Working Group, 2015: Elevation-dependent warming in mountain regions of the world. *Nature Climate Change*, **5**, 424-430, doi:10.1038/nclimate2563.

Neelin, J. D., and N. Zeng, 2015: A quasi-equilibrium tropical circulation model—Formulation. *J. Atmos. Sci.*, **57**, 1741-1766, doi:10.1175/1520-0469(2000)057<1741:AQETCM>2.0.CO;2.

Nie, J., W. R. Boos, and Z. M. Kuang, 2010: Observational Evaluation of a Convective Quasi-Equilibrium View of Monsoons. *J. Climate*, **23,** 4416-4428, doi:10.1175/2010JCLI3505.1.

Pierrehumbert, R. T., 2010: *Principles of planetary climate.* Cambridge University Press.

Popke, D., B. Stevens, and A. Voigt, 2013: Climate and climate change in a radiative-convective equilibrium version of ECHAM6. *J. Adv. Model Earth Sy.*, **5,** 1-14, doi:10.1029/2012MS000191.

Rao, G. V., and S. Erdogan, 1989: The Atmospheric Heat-Source over the Bolivian Plateau for a Mean January. *Bound.-Lay. Meteorol.,* **46,** 13-33, doi:10.1007/BF00118444.

Richardson, M. I., and R. J. Wilson, 2002: A topographically forced asymmetry in the martian circulation and climate. *Nature,* **416,** 298-301, doi:10.1038/416298a.

Romps, D. M., 2011: Response of Tropical Precipitation to Global Warming. *J. Atmos. Sci.,* **68,** 123-138, doi:10.1175/2010JAS3542.1.

Satoh, M., 1994: Hadley Circulations in Radiative-Convective Equilibrium in an Axially-Symmetrical Atmosphere. *J. Atmos. Sci.,* **51,** 1947-1968, doi:10.1175/1520-0469(1994)051<1947:HCIREI>2.0.CO;2.

Schneider, T., 2006: The general circulation of the atmosphere. *Annu. Rev. Earth Planet. Sci.*, **34,** 655-688, doi:10.1146/annurev.earth.34.031405.125144.

Sherwood, S. C., W. Ingram, Y. Tsushima, M. Satoh, M. Roberts, P. L. Vidale, and P. A. O'Gorman, 2010: Relative humidity changes in a warmer climate. *J. Geophys. Res.-Atmos.*, **115**, D09104, doi:10.1029/2009JD012585.

Silvers, L., B. Stevens, T. Mauritsen, and M. A. Giorgetta, 2016: Radiative convective equilibrium as a framework for studying the interaction between convection and its large-scale environment. *J. Adv. Model Earth Sy.*, **8**, doi:10.1002/2016MS000629.

Soden, B. J., and I. M. Held, 2006: An assessment of climate feedbacks in coupled ocean-atmosphere models. *J. Climate*, **19,** 3354-3360, doi:10.1175/JCLI3799.1.

Staff Members of Academia Sinica, 1958: On the General Circulation over Eastern Asia III. *Tellus*, **10,** 299-312, doi:10.1111/j.2153-3490.1958.tb02018.x.

Tao, W. K., J. Simpson, C. H. Sui, C. L. Shie, B. Zhou, K. M. Lau, and M. Moncrieff, 1999: Equilibrium states simulated by cloud-resolving models. *J. Atmos. Sci.*, **56,** 3128-3139, doi:10.1175/1520-0469(1999)056<3128:ESSBCR>2.0.CO;2.

Wu, G., and Y. Zhang, 1998: Tibetan Plateau forcing and the timing of the monsoon onset over South Asia and the South China Sea. *Monthly weather review*, 126(4), 913-927.

Wu, G. X., and Coauthors, 2007: The influence of mechanical and thermal forcing by the Tibetan Plateau on Asian climate. *J. Hydrometeorol.*, **8,** 770-789, doi:10.1175/JHM609.1.

Yanai, M., C. Li, and Z. Song, 1992: Seasonal heating of the Tibetan Plateau and its effects on the evolution of the Asian summer monsoon. *J. Meteor. Soc. Japan*, 70, 319-351

Yanai, M., and G. X. Wu, 2006: Effects of the Tibetan Plateau, in *The Asian Monsoon*, edited by B. Wang, Springer, 513-549.

822 Ye, D. Z., and G. X. Wu, 1998: The role of the heat source of the Tibetan Plateau in the general
823 circulation. *Meteorology and Atmospheric Physics*, 67(1), 181-198.
824 Zaitchik, B. F., J. P. Evans, and R. B. Smith, 2007: Regional impact of an elevated heat source:
825 The Zagros Plateau of Iran. *J. Climate*, **20,** 4133-4146, doi:10.1175/JCLI4248.1.

826 **Table 1:** Comparison of the two approaches to calculating orographic elevated heating [a]

Reference state	$T_{s,ref}$ (°C)	ΔR_{TOA} (W m^{-2})	$\Delta T_{s,est}$ (°C)	$T_{s,est}$ (°C)	$T_{s,eq}$ (°C)
Invariant T_s	28.0	-19.9	-10.0	18.0	19.4
T_s follows adiabat	5.0	+29.8	+14.9	19.9	19.4

827

828 [a] Offline calculations are performed for the case with a 0.24 surface albedo and with a surface
829 lifted from 1000 hPa to 500 hPa. The equilibrium surface temperature for the non-elevated case
830 is about 28°C. $T_{s,ref}$ represents the reference surface temperature assumed in either approach after
831 the surface is elevated. ΔR_{TOA} represents the TOA radiative flux change after the surface lifting,
832 and it can then be used to estimate surface temperature change $\Delta T_{s,est}$ using climate feedback.
833 $T_{s,est}$ is the estimated equilibrium surface temperature, that is, $T_{s,est} = T_{s,ref} + \Delta T_{s,est}$. $T_{s,eq}$
834 represents the final equilibrium surface temperature simulated by the full single-column model;
835 A single equilibrium solution is found for $T_{s,eq}$ with no evidence for multiple equilibria. Details
836 are discussed at the end of Section 5.

Figure Captions

Figure 1: (a) Equilibrium temperature profiles from cloud system-resolving simulations with various surface elevations but the same surface albedo of 0.24. Colored dots indicate the surface temperature for the corresponding case; the black dashed line marks the theoretical estimate of surface temperature obtained from our cloud-free single-column model (see text for details), with its slope based on surface elevations of 0 km and 6 km. (b) Upper tropospheric (200-400 hPa averaged) saturation equivalent potential temperatures versus subcloud (25 hPa above surface) equivalent potential temperatures for the simulations shown in panel a (red circles) and for the simulations with different surface albedos discussed in Section 6 (gray markers; crosses and triangles are for surface elevations of 0 km and 4 km, respectively). The black solid one-to-one line corresponds to the strict quasi-equilibrium assumption.

Figure 2: (a) Theoretical moist pseudoadiabats starting from surface elevations of 0 km (solid line) and 5 km (dashed line), together with the moist pseudoadiabatic lapse rate (colors). Numbers on the pseudoadiabats indicate the height in km above each surface, with circles shown every 2 km. (b) The same pseudoadiabats as in panel a but plotted in height coordinates, with the vertical axis indicating the height above each surface. (c) Vertical profile of the temperature difference between moist pseudoadiabats over surfaces with surface pressures of 1000 and 500 hPa, starting at surface temperatures of 5 °C (blue) and 15 °C (red). Note the greater temperature difference in the warmer climate, particularly in the upper troposphere.

Figure 3: Elevated radiative forcing when the surface is elevated from 1000 hPa to 500 hPa with a fixed albedo of 0.24, for each term in Eq. (14). R_{ADD} is for the addition of the four terms, and R_{NET} is the net radiative forcing change with all the aforementioned effects and their interactions.

Figure 4: (a) Vertical profiles of the temperature change from the case with an unchanged temperature profile *T(z)* to the case with a new pseudoadiabat, when the surface is elevated from 1000 hPa to 500 hPa, with a fixed surface temperature of 28°C (yellow) and 20°C (green). (b) The lapse rate effect on OLR (i.e. $LW_{LAPSE+H2O}$) after the removal of the temperature difference above a certain level; for example, the value at 100 hPa corresponds to the case with the removal of all temperature differences above the level 100 hPa in the radiative flux calculation. Yellow lines correspond to the case presented in Fig. 3. Both quantities are plotted in pressure coordinates of the elevated case (i.e. surface pressure = 500 hPa), and dots represent the 26 equispaced pressure levels in the offline radiative calculations. Note the contribution of the stratosphere/upper troposphere to the lapse rate effect becomes stronger in a warmer climate.

Figure 5: Contributions to the net top-of-atmosphere (TOA) radiative flux change (W/m^2) when the surface is elevated from the reference level (surface pressure 1000 hPa) to the target level indicated on the vertical axis while surface temperature is fixed at value indicated on the horizontal axis. Contributions are from (a) shortwave, (b) longwave due to changes in carbon dioxide optical path, (c) longwave due to changes in water vapor optical path at a fixed lapse rate, and (d) longwave due to lapse rate changes. Also shown are (e) the sum of (a-d), and (f) the net TOA radiative flux change including all aforementioned effects and their interactions.

Positive values indicate a warming effect and negative a cooling effect. The physical meaning of each term and the method of calculation are described in Section 5.

Figure 6: (a) Surface temperatures and (b) low-level equivalent potential temperatures over non-elevated surfaces (red) and over surfaces with 4 km elevation (blue), for a broad range of surface albedos, all from cloud system-resolving simulations of radiative-convective equilibrium. Note the greater surface temperature drop and the weaker elevated heating effect in warmer climates (i.e. those with lower surface albedos).

Figure 7: (a,b) Vertical profiles of (a) temperature and (b) temperature anomaly with respect to the 1.5 km case (i.e. 850 hPa surface pressure; see main text), for the simulations with surface albedo of 0.2; the legend indicates the surface elevation used for each curve. (c,d) Same as (a,b) but without radiatively-active clouds; temperature anomaly is with respect to the additional 1 km case.

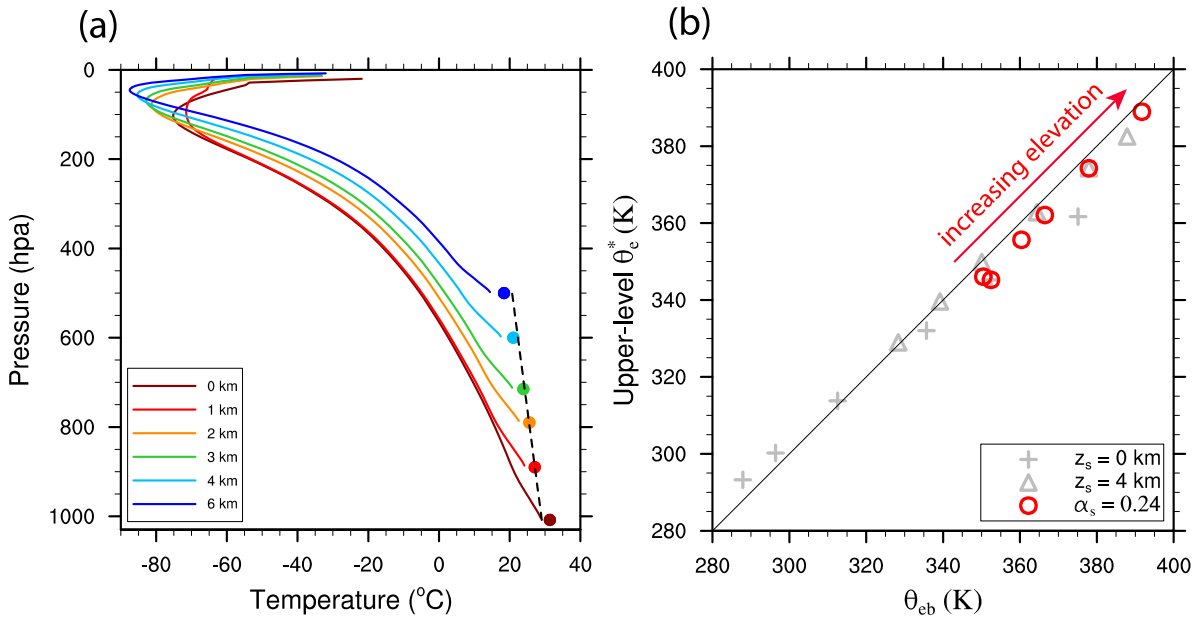

Figure 1: (a) Equilibrium temperature profiles from cloud system-resolving simulations with various surface elevations but the same surface albedo of 0.24. Colored dots indicate the surface temperature for the corresponding case; the black dashed line marks the theoretical estimate of surface temperature obtained from our cloud-free single-column model (see text for details), with its slope based on surface elevations of 0 km and 6 km. (b) Upper tropospheric (200-400 hPa averaged) saturation equivalent potential temperatures versus subcloud (25 hPa above surface) equivalent potential temperatures for the simulations shown in panel a (red circles) and for the simulations with different surface albedos discussed in Section 6 (gray markers; crosses and triangles are for surface elevations of 0 km and 4 km, respectively). The black solid one-to-one line corresponds to the strict quasi-equilibrium assumption.

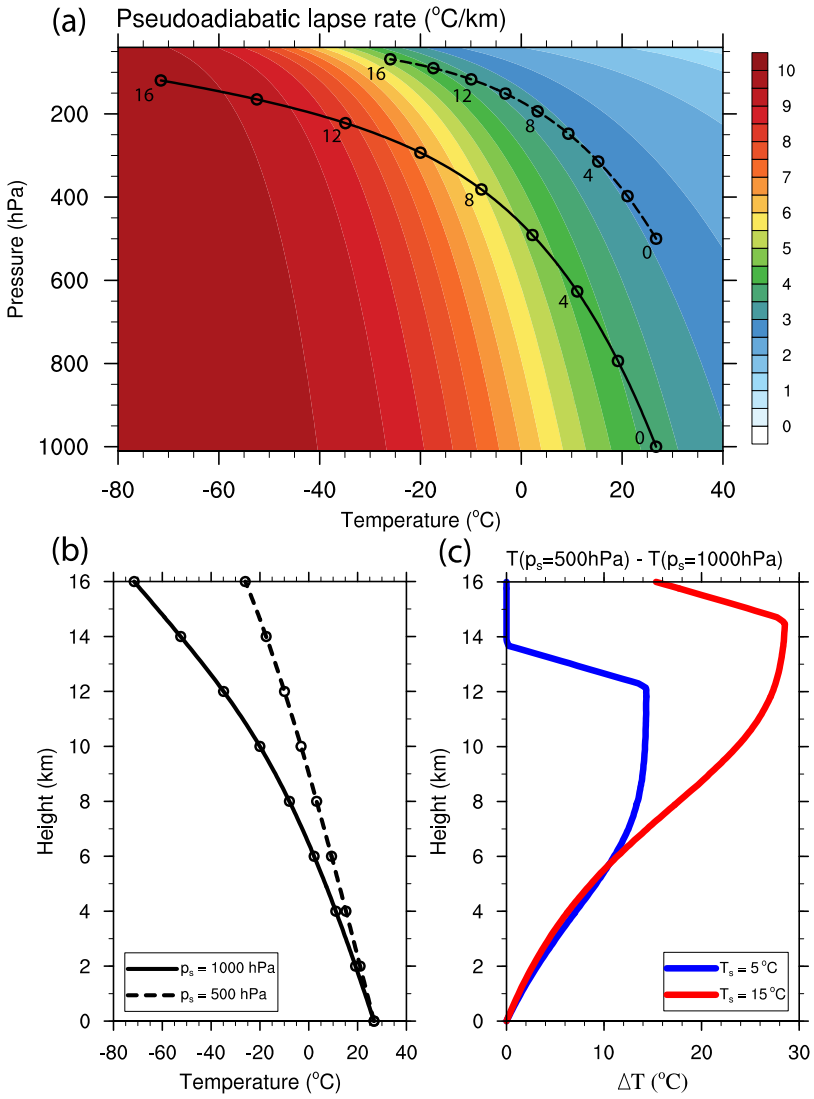

907

908 **Figure 2**: (a) Theoretical moist pseudoadiabats starting from surface elevations of 0 km (solid
909 line) and 5 km (dashed line), together with the moist pseudoadiabatic lapse rate (colors).
910 Numbers on the pseudoadiabats indicate the height in km above each surface, with circles shown
911 every 2 km. (b) The same pseudoadiabats as in panel a but plotted in height coordinates, with
912 the vertical axis indicating the height above each surface. (c) Vertical profile of the temperature
913 difference between moist pseudoadiabats over surfaces with surface pressures of 1000 and 500
914 hPa, starting at surface temperatures of 5 °C (blue) and 15 °C (red). Note the greater temperature
915 difference in the warmer climate, particularly in the upper troposphere.

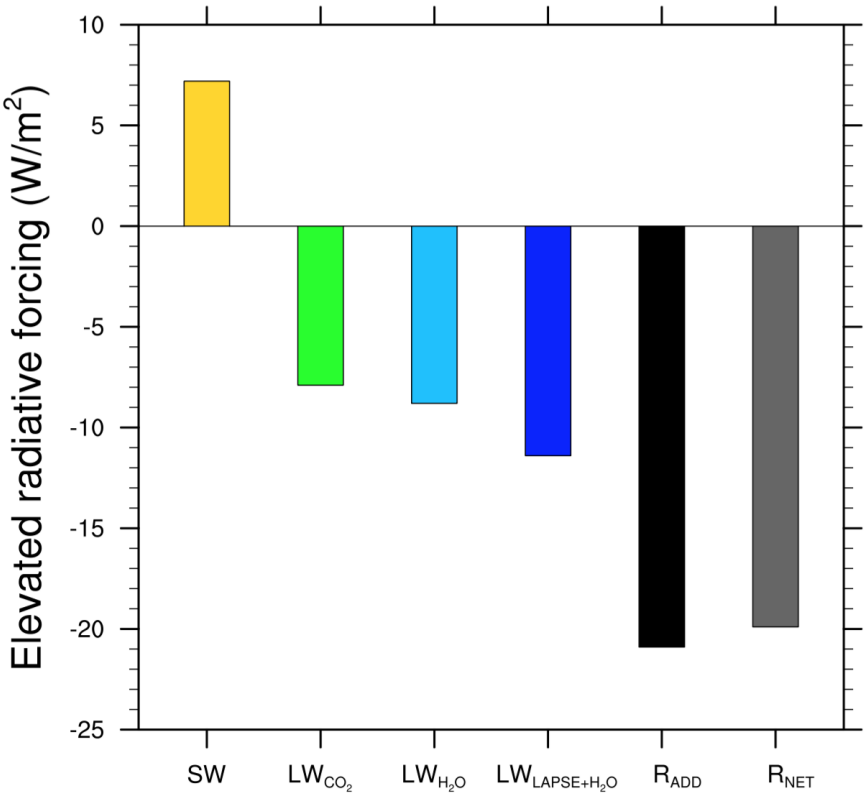

916

917 **Figure 3**: Elevated radiative forcing when the surface is elevated from 1000 hPa to 500 hPa with

918 a fixed albedo of 0.24, for each term in Eq. (14). R_{ADD} is for the addition of the four terms, and

919 R_{NET} is the net radiative forcing change with all the aforementioned effects and their interactions.

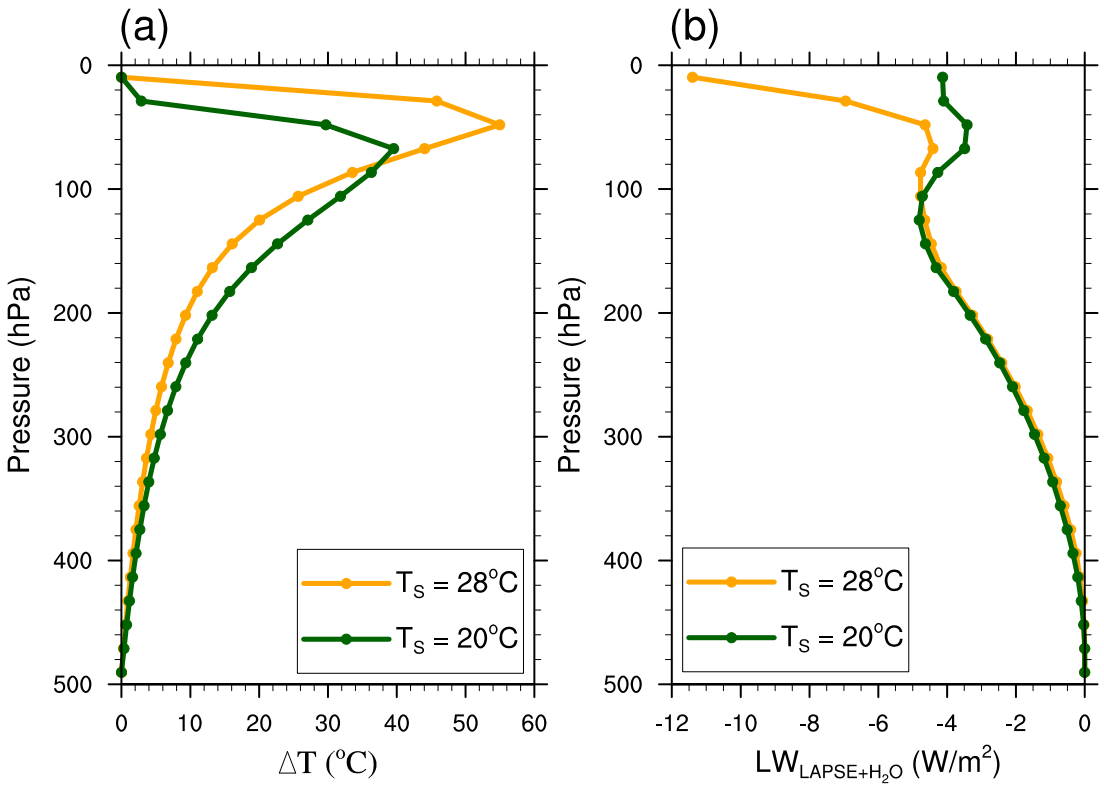

Figure 4: (a) Vertical profiles of the temperature change from the case with an unchanged temperature profile *T(z)* to the case with a new pseudoadiabat, when the surface is elevated from 1000 hPa to 500 hPa, with a fixed surface temperature of 28°C (yellow) and 20°C (green). (b) The lapse rate effect on OLR (i.e. $LW_{LAPSE+H2O}$) after the removal of the temperature difference above a certain level; for example, the value at 100 hPa corresponds to the case with the removal of all temperature differences above the level 100 hPa in the radiative flux calculation. Yellow lines correspond to the case presented in Fig. 3. Both quantities are plotted in pressure coordinates of the elevated case (i.e. surface pressure = 500 hPa), and dots represent the 26 equispaced pressure levels in the offline radiative calculations. Note the contribution of the stratosphere/upper troposphere to the lapse rate effect becomes stronger in a warmer climate.

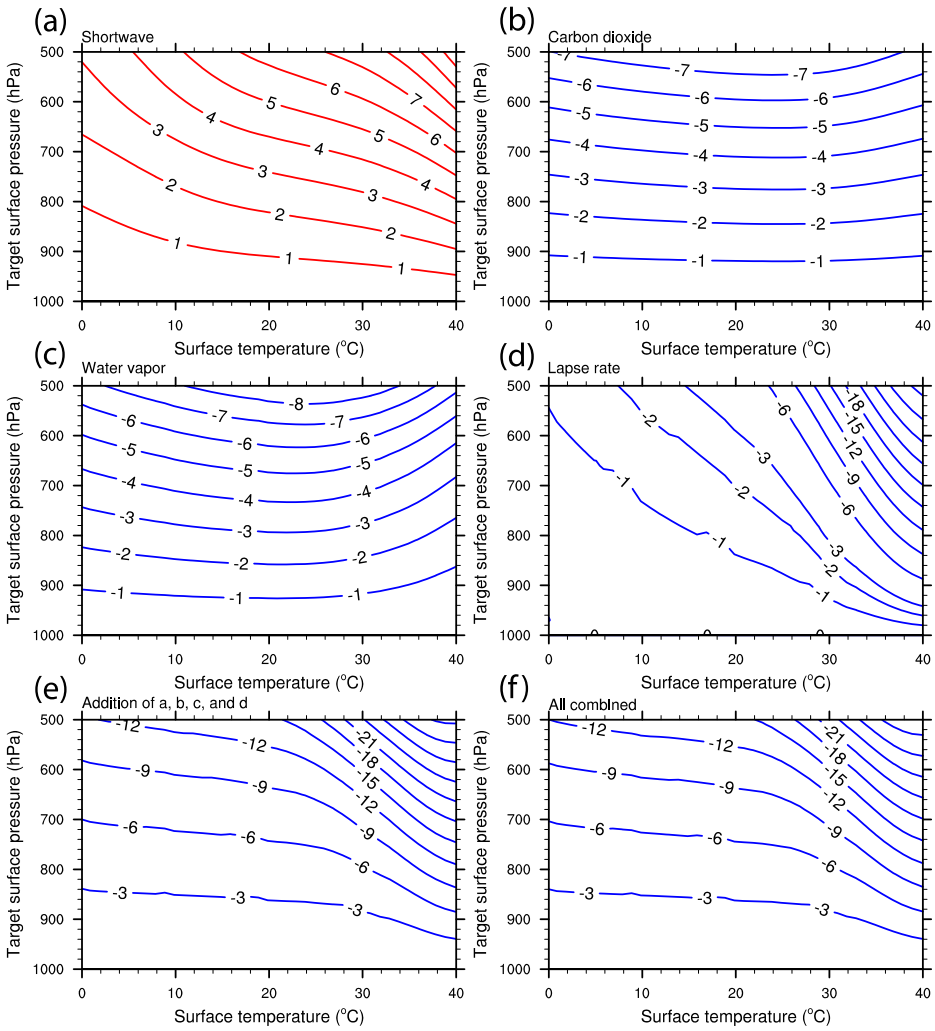

931

932 **Figure 5**: Contributions to the net top-of-atmosphere (TOA) radiative flux change (W/m^2) when
933 the surface is elevated from the reference level (surface pressure 1000 hPa) to the target level
934 indicated on the vertical axis while surface temperature is fixed at value indicated on the
935 horizontal axis. Contributions are from (a) shortwave, (b) longwave due to changes in carbon
936 dioxide optical path, (c) longwave due to changes in water vapor optical path at a fixed lapse
937 rate, and (d) longwave due to lapse rate changes. Also shown are (e) the sum of (a-d), and (f) the
938 net TOA radiative flux change including all aforementioned effects and their interactions.
939 Positive values indicate a warming effect and negative a cooling effect. The physical meaning of
940 each term and the method of calculation are described in Section 5.

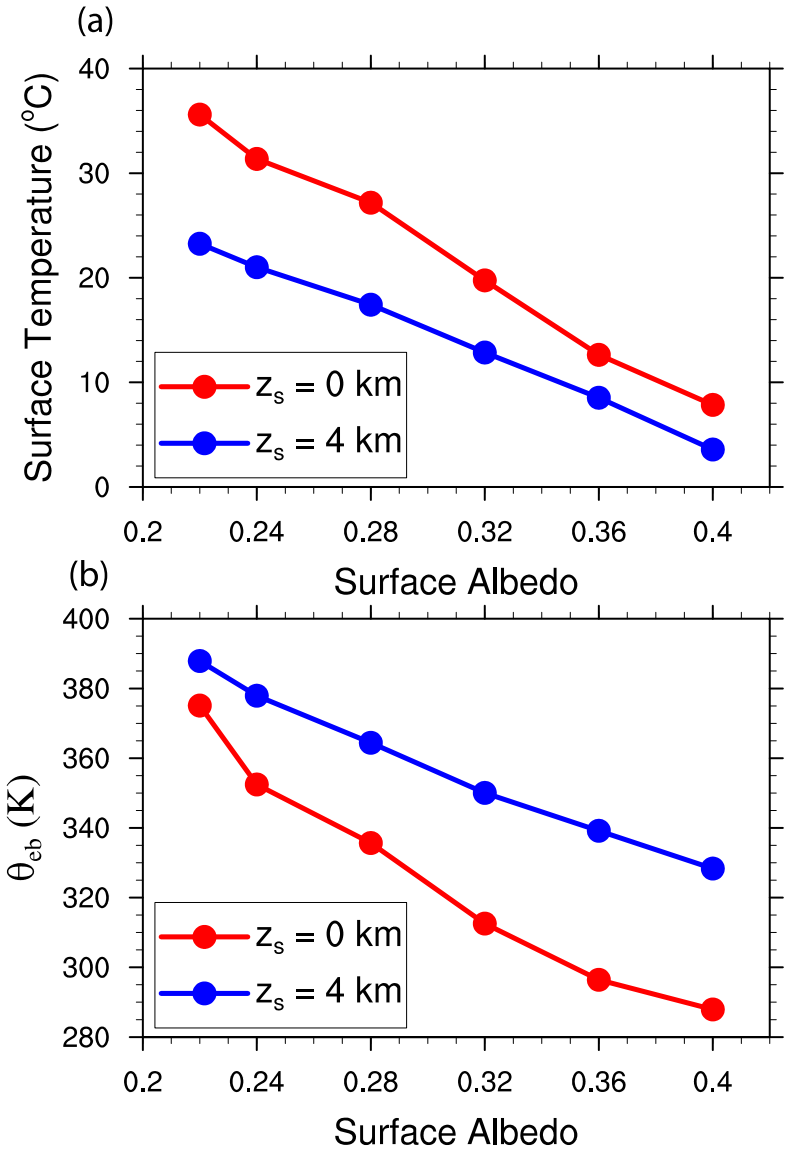

941

942 **Figure 6**: (a) Surface temperatures and (b) low-level equivalent potential temperatures over non-
943 elevated surfaces (red) and over surfaces with 4 km elevation (blue), for a broad range of surface
944 albedos, all from cloud system-resolving simulations of radiative-convective equilibrium. Note
945 the greater surface temperature drop and the weaker elevated heating effect in warmer climates
946 (i.e. those with lower surface albedos).

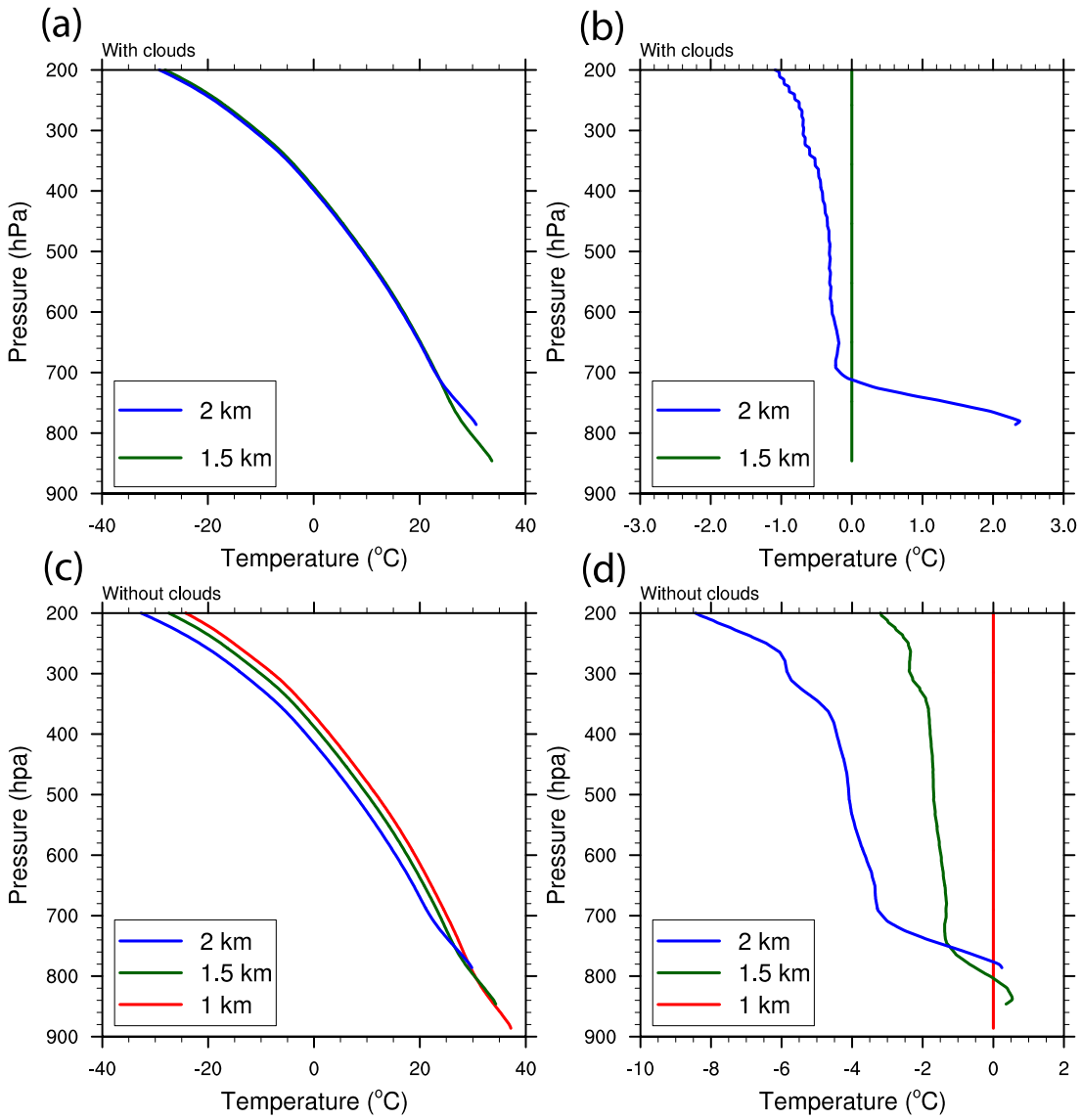

947

948 **Figure 7**: (a,b) Vertical profiles of (a) temperature and (b) temperature anomaly with respect to
949 the 1.5 km case (i.e. 850 hPa surface pressure; see main text), for the simulations with surface
950 albedo of 0.2; the legend indicates the surface elevation used for each curve. (c,d) Same as (a,b)
951 but without radiatively-active clouds; temperature anomaly is with respect to the additional 1 km
952 case.